Article ID: 1006-8775(2017) 01-0001-14

APPLICATIONS OF THE CLOUDSAT TROPICAL CYCLONE PRODUCT IN ANALYZING THE VERTICAL STRUCTURE OF TROPICAL CYCLONES OVER THE WESTERN PACIFIC

LI Guan-lin (李冠林)[1], YAN Wei (严 卫)[1], HAN Ding (韩 丁)[1], WANG Rui (王 蕊)[1], YE Jing (叶 晶)[2]
(1. College of Meteorology and Oceanography, PLA University of Science and Technology, Nanjing 211101 China;
2. Unit No.95871 of PLA, Hengyang, Hunan 421000 China)

Abstract: Cloud profiling radar (CPR) onboard CloudSat allows for deep penetration into dense clouds/precipitation. In this study, tropical cyclones (TCs) are classified into three stages as developing, mature, and decaying. The circular TC area with the radius of 500 km is divided into five regions. The vertical structure characteristics of 94 Western Pacific TCs at different stages in different regions from June 2006 to February 2014 are statistically quantified using the CloudSat tropical cyclone overpass product (the CSTC Product). Contoured frequency by altitude diagrams (CFADs) of radar reflectivity show an arc-like feature and exhibit opposite distributions with a boundary at 5 km. Bright bands are found at this altitude, indicating melting layers. Deep convective (DC) clouds have the largest occurrence probability in the inner region, while *Ci* clouds occur more frequently in the outer region at 10-15 km. *As* clouds have the second largest vertical scale after DC clouds. Distributions of *Ac*, *Cu*, and *Ns* clouds at different stages have few distinctions. As the altitude increases, the ice effective radius and the distribution width parameter decrease while the particle number concentration increases. Moist static energy (MSE), cloud thickness (CT), liquid water path (LWP), ice water path (IWP), water vapor (WV), and rain rate (RR) all diminish along the radial direction and are significantly larger at the mature stage. The average value of MSE at the developing stage is larger than that at the decaying stage.

Key words: CPR; CloudSat; tropical cyclone; vertical structure; statistical analysis
CLC number: P444 **Document code:** A
doi: 10.16555/j.1006-8775.2017.01.001

1 INTRODUCTION

Tropical cyclones (TCs) cause extensive damage to oceangoing voyages, offshore aquaculture, marine resources exploitation, as well as aerospace and military activity. Meanwhile, strong precipitation caused by TCs helps to relieve drought conditions. The Western Pacific is the area TCs occur most frequently, whose annual number accounts for 33% of the total in the world (Chan[1]). China is one of the countries that suffer from TCs most severely. At present, most research focuses on occurrence frequency (Landsea et al.[2]; Zhan et al.[3]), evolution features (Dunion et al.[4]), intensity estimation (Luo et al.[5]; Wong and Emanuel[6]), and track forecasting (Cheung[7]; Poroseva et al.[8]). A more detailed understanding of macro- and micro- physical characteristics is desperately needed.

TCs form and develop over the warm tropical oceans. Due to the scarcity of in situ observations in the past, TCs are difficult to analyze and predict. Satellite-based remote sensing is a superb method for performing structure analysis. Conventional satellite observations (e.g., passive visible-infrared sensors and microwave spectrum radiometers) have a long history of use in investigating TCs (Dvorak [9]; Rodgers et al.[10]; Kidder et al.[11]). However, these instruments are limited to statements on cloud-top properties. Previous studies have demonstrated that the vertical structure plays a vital role in the dynamics of TCs (Stern and Nolan[12]; Hence and Houze[13]; Hence and Houze[14]; Miller et al.[15]). Kovacs and Mccormick provided the first high-resolution (15 m) vertical profiling of clouds, aerosols, and precipitation within the eye, eyewall, and cirrus shield of Typhoon Melissa [16]. This high-resolution product was based on data from the Lidar In-Space Technology Experiment (LITE). However, LITE's performance is inherently affected by the presence of thick clouds/precipitation. Therefore, low altitude details are easily missed. Yokoyama and Takayabu statistically quantified the three-dimensional rain characteristics of TCs using the Tropical Rainfall Measuring Mission (TRMM) data from December 1997 to December 2003[17]. TRMM is limited to observing precipitation-size particles and cannot detect cloud particles.

Received 2016-03-22; **Revised** 2017-01-09; **Accepted** 2017-02-15
Foundation item: National Natural Science Foundation of China (41076118); Young Scientists Fund of National Natural Science Foundation of China Grant (41005018)
Biography: LI Guan-lin, Ph. D., Associate Researcher, primarily undertaking research on cloud physics.
Corresponding author: YAN Wei, e-mail: 18913979082@163.com

21994-2017 China Academic Journal Electronic Publishing House. All rights reserved. http://www.cnki.net

CloudSat was launched on 28 April 2006, equipped with the first spaceborne W-band (94 GHz; 3.2 mm) cloud profiling radar (CPR) as the only payload instrument. By measuring the backscattered signal every 240 m along its path, CPR provides an unprecedented perspective of cloud condensate and precipitation. The distinctive feature of CPR lies in its ability to penetrate optically thick clouds (Stephens et al. [18]). Therefore, CPR can provide the detailed inner structure of clouds and precipitation for complicated weather systems such as TCs. CloudSat flies in formation with the afternoon satellite constellation referred to as the A-Train constellation (Stephens et al. [19]). The A-Train is a collection of active and passive sensors that operate in different wave bands and offer near simultaneous observations. The A-Train constellation combines data from different satellite sources for further research on internal physical structure and dynamic mechanism of TCs. Recently conducted research on TCs using data from the A-Train constellation has mostly concentrated on case studies. Mitrescu et al. analyze the cloud and precipitation structures of Hurricane Ileana and Typhoon Durian [20]. The study showed that some strong convective cores could be clearly depicted by CloudSat and the traditional method of geostationary satellites was not able to present such performance. Matrosov retrieved rainfall and ice content parameters of two major TCs from the 2008 season (Gustav and Ike [21]). Their results are in reasonable agreement with estimates from surface precipitation radar sensors and may complement measurements from other traditional satellite sources. Durden et al. discussed the cloud structure of six TCs in detail and then combined seventeen cases to statistically analyze the contoured frequency by altitude diagrams (CFADs, Yuter and Houze [22]) of radar reflectivity, cloud classification, and ice parameters in eyewall and stratiform regions [23]. All of these studies have made significant contributions, but their limited sample sizes may not entirely represent the general characteristics of TCs. Thus, more data are needed to draw definitive conclusions.

During the period from June 2006 to February 2014, nearly 8,000 CloudSat overpasses of TCs were collected within 1,000 km of the storm center. The purpose of this study is to examine the vertical structure characteristics of TCs with different intensity levels at different stages. A better understanding of TC structure characteristics may also lead to eventual improvements in the size, rainfall, and storm surge predictions.

The structure of this paper is as follows. Section 2 gives a brief description of the CSTC Product and the method adopted for statistical analysis. Section 3 details the vertical structure characteristics of TCs, including radar reflectivity, cloud occurrence probability, ice cloud parameters, and moist static energy. In section 4 we synthesize the results and draw conclusions.

2 DATA AND METHODOLOGY

The Level 2-D Tropical Cyclone Product (hereafter referred to as the CSTC Product) is used in this study (Tourville et al. [24]). The CSTC Product is provided by the United States Naval Research Laboratory (NRL) and the CloudSat Data Processing Center (DPC). The CSTC Product contains all CloudSat overpasses within 1,000 km of a named TC over six basins (the Atlantic, East Pacific, Center Pacific, West Pacific, Indian Ocean, and Southern Hemisphere). From June 2006 to February 2014, 7,988 overpasses were collected, of which 382 are within 50 km of the storm center. Now CloudSat only operates during the daytime after a spacecraft battery anomaly. The CSTC Product combines CloudSat observations with Moderate Resolution Imaging Spectroradiometer (MODIS), Advanced Microwave Scanning Radiometer-Earth Observing System (AMSR-E), Cloud Aerosol with Orthogonal Polarization (CALIOP), Navy Operational Global Atmospheric Prediction System (NoGAPS), European Centre for Medium-Range Weather Forecasts (ECMWF), and the best track data presented by different meteorological institutions all over the world. Detailed best track data is downloaded from Unisys Weather as this data is seriously lacking in the CSTC Product. A list of datasets used in this paper is summarized in Table 1. More detailed information on the CSTC product can be found at the DPC website: http://cloudsat.cira.colostate.edu.

In order to analyze structural changes of TCs at different evolutionary stages during their life cycles, We adopt the method from Yokoyama and Takayabu to determine three life stages for each TC (i.e., developing, mature, and decaying)[17]. The mature stage is defined as the period when the maximum sustained wind (MSW) exceeds an 80% threshold of the system's peak intensity. The periods before and after the mature stage are the developing stage and the decaying stage, respectively. If a TC develops again after the first decaying stage, we treat the TC as two separate TCs.

Based on the Saffir-Simpson hurricane wind scale (SSHWS), TCs are classified into the seven categories of tropical depression (TD), tropical storm (TS), and categories 1–5 (C1–C5) (Kantha [25]). In this study, we use data satisfying the following criteria: 1) the TC intensity is at C1 or above (MSW>33 m/s); 2) the distance between the nadir point and the storm center is less than 500 km; 3) the TC is from the Western Pacific. It should be noted that we do not take into account the variation in TC size. Nevertheless, this is probably not a major concern because we are mostly interested in outlining the radial structure. There are a variety of ways to measure TC size, such as ROCI (the radius of the outer closed isobar from the surface synoptic charts) and R34 (the average radius of 34 kt (1 kt = 0.514 m/s) surface wind). But no universally accepted definition exists (Chan and Yip [26]). Based on

21994-2017 China Academic Journal Electronic Publishing House. All rights reserved. http://www.cnki.net

Table 1. Detailed information on the CSTC product.

Type	Description	Parameters
2B-GEOPROF	Cloud geometric profile product	CPR cloud mask, radar reflectivity and gaseous attenuation
2B-GEOPROF-LIDAR	2B-GEOPROF and CALIOP lidar correlated observations	Cloud layer number and cloud boundary height from combined CPR and CALIOP
2B-CLDCLASS	Eight types of clouds	Cloud classification
2B-CWC	liquid/ice microphysical parameters	Liquid/ice water content, water path, effective radius, number concentration, distribution width parameter
2C-PRECIP-COLUMN	Estimate of surface precipitation from CS CPR reflectivity profiles and temperature and humidity data from ECMWF auxiliary dataset	Frozen precipitation height, precipitation intensity, and freezing level height
ECMWF-AUX	Auxiliary ECMWF data sampled along CS track	Temperature, pressure, and specific humidity from ECMWF
MODIS-AUX	MODIS data matched to the CS footprint	Brightness temperature, cloud top height, and cloud top pressure
AMSR-E	AMSR-E levels 2A and 2B data matched to the CS footprint	Brightness temperature, wind speed, SST, cloud water content, atmospheric water vapor content, and rain rate
Best track data	Best track data from different meteorological institutions	Latitude, longitude, minimum sea level pressure(MSLP), and maximum sustained wind (MSW)
Storm specific information	Reynolds storm center SST, and GFS wind shear (200-850 hPa)	Strom center SST, and wind shear

different definitions, previous statistical studies have shown that the mean TC size over the Pacific varies from ~200 km to ~500 km (Chan and Chan [27]; Chan and Yip[26]; Chavas and Emanuel[28]; Wada et al.[29]; Liu and Chan [30]). Thus, we adopt a TC size of 500 km. Eventually, we obtain 94 TCs, 683 granules, and 477,342 profiles. The long-term statistics offered by CPR compensate for the lack of time continuity in the data on any one TC. Table 2 gives detailed information regarding the 94 TCs used in this study (only SSHWS $\geqslant$ 4 are shown due to limited space). The minimum distance (Min Dis) is the distance between the storm center and the CPR beam's closest approach. The minimum sea level pressure (MSLP), MSW, CloudSat granule number (GraNum), and SSHWS are also listed in Table 2.

The circular TC area with the radius of 500 km is divided into 100 km bins: the 0-100 km circular region (A1 region), the 100-200 km annular region (A2 region), the 200-300 km annular region (A3 region), the 300-400 km annular region (A4 region), and the 400-500 km annular region (A5 region). The distribution characteristics of the data used in this study are shown in Fig.1. The numbers of granules and profiles (in parentheses) in each region at each stage are listed in Table 3. It can be seen that the numbers at each stage increase from the A1 to A5 region.

3 RESULTS AND ANALYSIS

3.1 *Radar reflectivity*

Figure 2 shows the CFAD of radar reflectivity at each stage in each region. All CFADs in the 15 panels are characterized by an arc-like feature, similar to that seen in previous studies on a Madden-Julian Oscillation (Masunaga et al. [31]) and deep convective clouds (Dodson et al.[32]). Radar reflectivity is an indicator of particle size and helps to determine the phase. The "arc" is divided into two branches by a bright band at approximately 5 km, indicating the existence of a melting layer (Sassen et al.[33]). The bright band results from a growth in the water dielectric constant occurring from the shift from the ice phase to the liquid phase. For non-precipitating clouds, hydrometeors are sufficiently small and behave as Rayleigh scatterers at the CPR wavelength. In the Rayleigh scattering regime, radar reflectivity is proportional to the sixth power of the particle diameter. Radar reflectivity increases along the upper branch of the arc with decreasing altitude, in accordance with the increasing ice effective radius in Fig.5c and 5d. Large values above the melting layer indicate the presence of large ice particles or supercooled liquid water droplets (Huang et al.[34]). *As* the hydrometeor diameter increases, radar scattering moves into the Mie scattering regime. Along the lower branch toward the ground, the relationship between radar reflectivity and altitude reverses. Radar reflectivity declines rapidly due to strong rain attenuation. Such reduction is not seen in CFADs of TRMM measurements (Houze [35]). The radar reflectivity of rain is typically 10-50 dBZ. In Fig.2, peak values vary little among all 15 CFADs, reaching up to approximately 17 dBZ. These values are much less than those observed at longer wavelengths.

At the mature stage, strong reflectivities (e.g., >15 dBZ) stretch from 5 km to 13 km in the A1 region. This indicates strong convection. A mass of supercooled

21994-2017 China Academic Journal Electronic Publishing House. All rights reserved. http://www.cnki.net

Table 2. Detailed information on TCs overpassed by CloudSat over the Western Pacific from June 2006 to February 2014 (only SSHWS≥4).

index	year	name	MSLP	MSW (kn)	MinDist	GraNum	SSHWS
1	2006	EWINIAR	916	130	28	22	4
2	2006	SAOMAI	898	140	83	21	5
3	2006	SHANSHAN	922	120	78	21	4
4	2006	YAGI	898	140	40	23	5
5	2006	XANGSANE	997	125	284	11	4
6	2006	CIMARON	898	140	47	29	5
7	2006	CHEBI	927	115	10	31	4
8	2006	DURIAN	916	135	0	29	4
9	2007	YUTU	922	125	33	24	4
10	2007	MAN-YI	922	135	130	24	4
11	2007	USAGI	933	120	11	18	4
12	2007	SEPAT	922	140	45	17	5
13	2007	NARI	937	120	15	15	4
14	2007	WIPHA	926	135	95	13	4
15	2007	KROSA	926	130	60	15	4
16	2008	RAMMASUN	926	135	134	18	4
17	2008	NAKRI	929	125	21	8	4
18	2008	SINLAKU	929	125	29	28	4
19	2008	HAGUPIT	933	125	47	19	4
20	2008	JANGMI	904	140	20	14	5
21	2009	KUJIRA	937	115	21	17	4
22	2009	VAMCO	931	120	32	22	4
23	2009	CHOI-WAN	918	140	23	18	5
24	2009	PARMA	926	135	38	32	4
25	2009	MELOR	914	150	13	23	5
26	2009	LUPIT	919	140	22	27	5
27	2009	NIDA	903	155	8	24	5
28	2010	MEGI	907	155	24	21	5
29	2010	CHABA	937	115	74	21	4
30	2012	GUCHOL	926	130	314	7	4
31	2012	VICENTE	978	115	159	3	4
32	2012	TEMBIN	948	115	145	11	4
33	2012	BOLAVEN	929	125	75	8	4
34	2012	SANBA	941	150	138	6	5
35	2012	JELAWAT	918	140	43	10	5
36	2012	BOPHA	918	140	56	13	5
37	2013	SOULIK	944	125	84	7	4
38	2013	UTOR	948	130	21	8	4
39	2013	USAGI	933	140	303	5	5
40	2013	DANAS	959	125	453	3	4
41	2013	WIPHA	956	115	128	6	4
42	2013	FRANCISCO	922	140	5	7	5
43	2013	LEKIMA	918	140	151	5	5
44	2013	HAIYAN	903	170	96	8	5

21994-2017 China Academic Journal Electronic Publishing House. All rights reserved. http://www.cnki.net

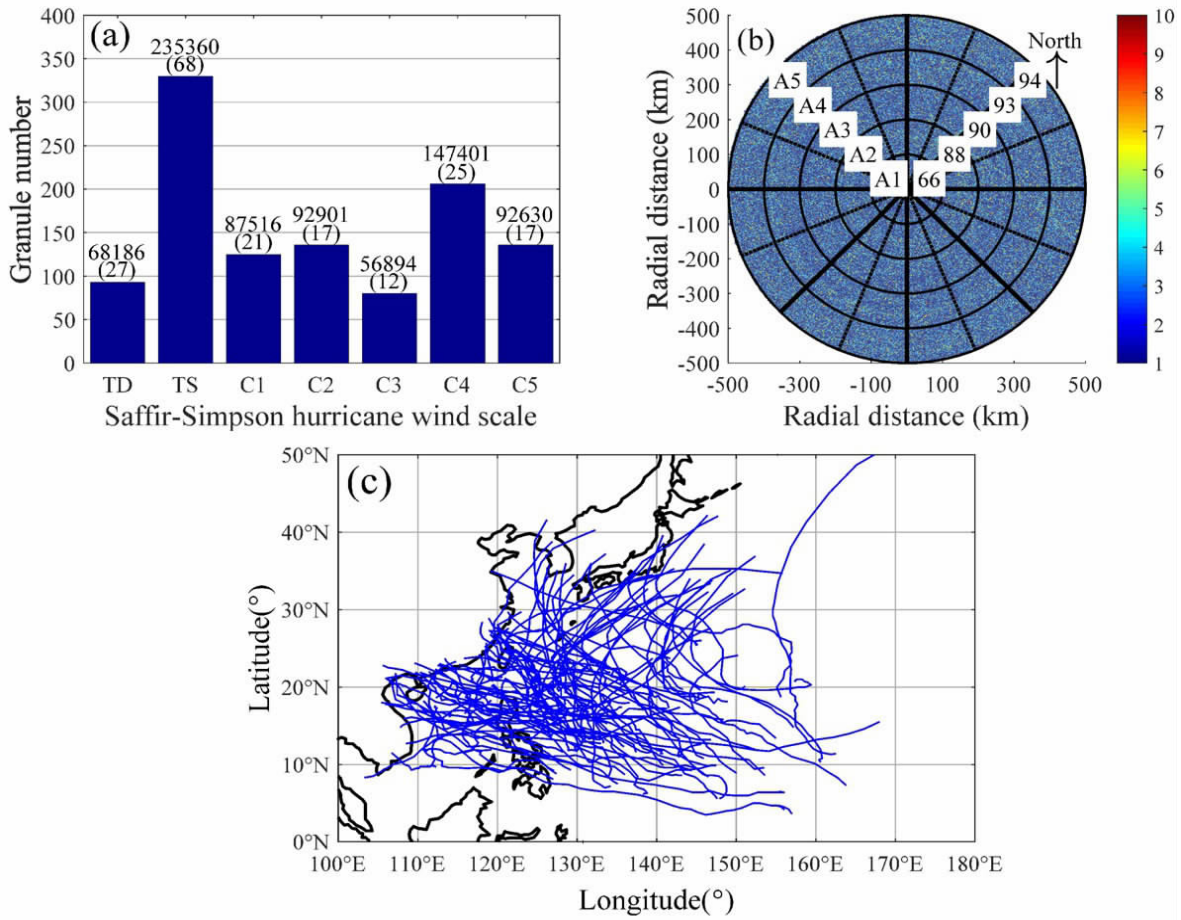

Figure1. The distribution characteristics of the data used in this study. (a) The intensity distribution. The abscissa indicates the SSHWS and the ordinate indicates the number. The numbers of granules and TCs (in parentheses) of each intensity scale are labeled above the column bar. (b) The profile distribution. The circular TC area is divided into five regions (A1-A5). The origin of coordinates represents the storm center, and x and y are the eastward and northward coordinates, respectively. The color indicates the number of profiles in a pixel with a resolution of 2 km × 2 km. The number of TCs in each region is also labeled. (c) Best tracks of the 94 TCs during the lifetime.

Table 3. The numbers of granules and profiles (in parentheses) in each section at each stage.

Stages	A1 region	A2 region	A3 region	A4 region	A5 region
Developing	64 (9028)	155 (34382)	212 (49490)	298 (74006)	386 (98840)
Mature	19 (2810)	39 (7762)	63 (15839)	87 (22385)	119 (32583)
Decaying	46 (6383)	77 (15974)	109 (26032)	148 (37517)	178 (44311)

liquid water droplets and ice particles concentrate in this altitude. At the other two stages, the vertical scales are smaller. The convection gradually vanishes with increases in the radial distance. In the A3-A5 regions below 5 km, the probability of large reflectivity (e.g., >0 dBZ) is smaller at the mature stage than those at the other two stages, while above 10 km the probability of small reflectivity (e.g., <0 dBZ) is larger at the mature stage than those at the other two stages. This may be due to the stronger convergence and divergence at the mature stage. Liquid water droplets are transported from the outer region to the inner region at low altitudes while ice particles are transported in an opposite direction at high altitudes (Houze [35]).

From the A1 to A5 region at all three stages, large probabilities tend to shift from large reflectivities (e.g., >0 dBZ) in the lower branch to small reflectivities (e.g., <0 dBZ) in the upper branch, which coincides with what can be seen in Fig.4. Above 10 km, deep convective clouds with corresponding large reflectivities dominate cirrus clouds with corresponding small reflectivities in the A1 and A2 regions, while the relationship reverses in the A4 and A5 regions.

Figure 3 shows the spatial distribution of mean radar reflectivity along the radial direction at each stage. A bright band can be seen in each panel at approximately 5 km. The dark red area represents intensive convection and is more apparent at the mature

21994-2017 China Academic Journal Electronic Publishing House. All rights reserved. http://www.cnki.net

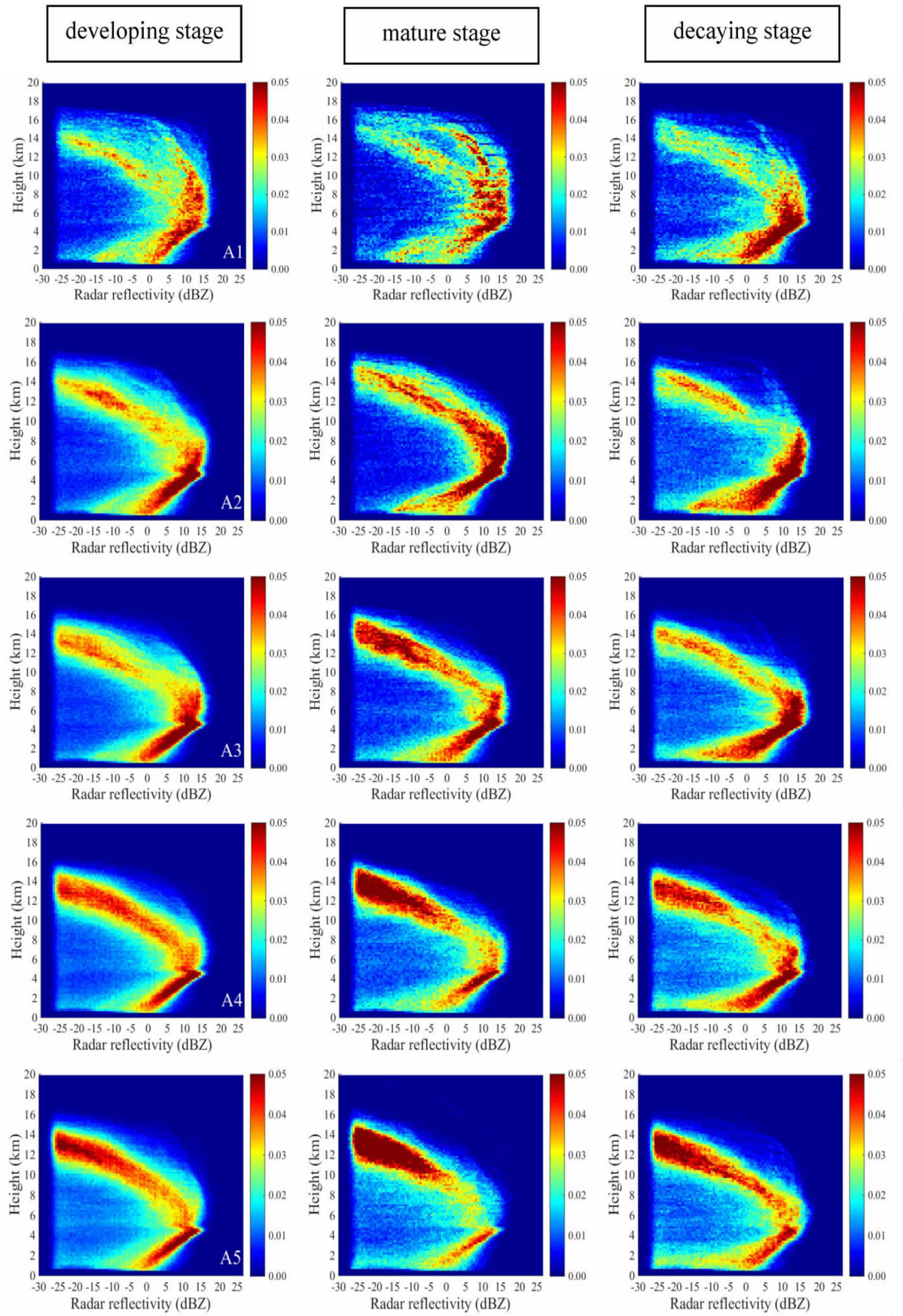

Figure 2. CFADs of CloudSat radar reflectivity. Each row represents one region and each column represents one stage.

21994-2017 China Academic Journal Electronic Publishing House. All rights reserved. http://www.cnki.net

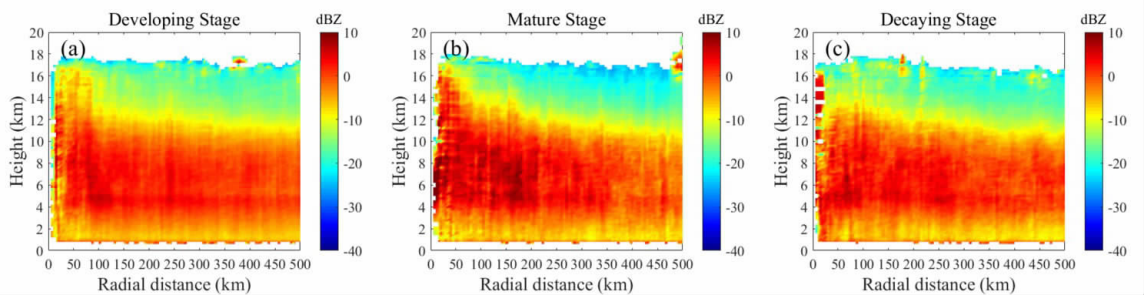

Figure 3. Spatial distributions of radar reflectivity along the radial direction at (a) the developing stage, (b) the mature stage, and (c) the decaying stage.

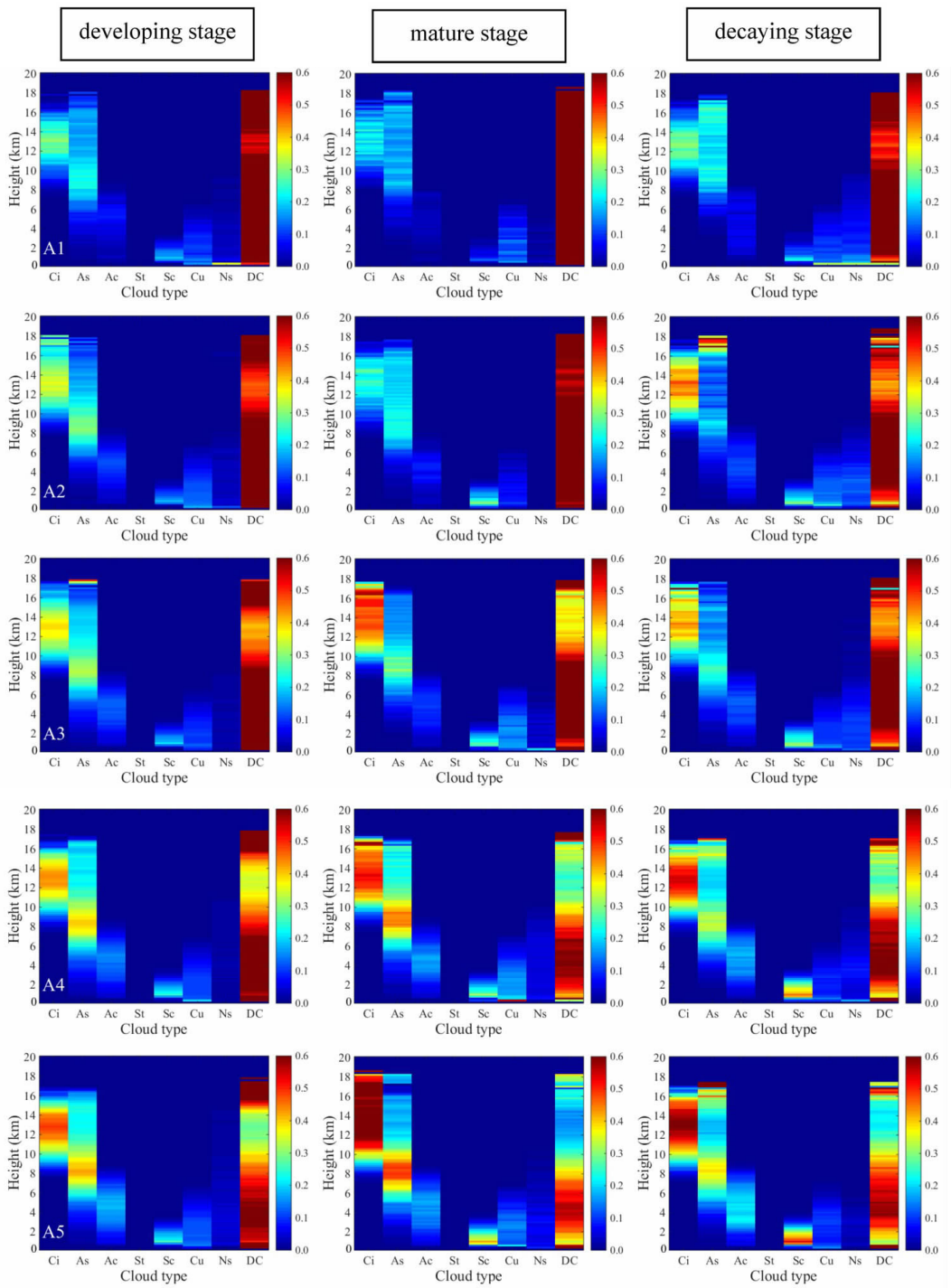

Figure 4. CFADs of cloud classification. Each row represents one region and each column represents one stage.

21994-2017 China Academic Journal Electronic Publishing House. All rights reserved. http://www.cnki.net

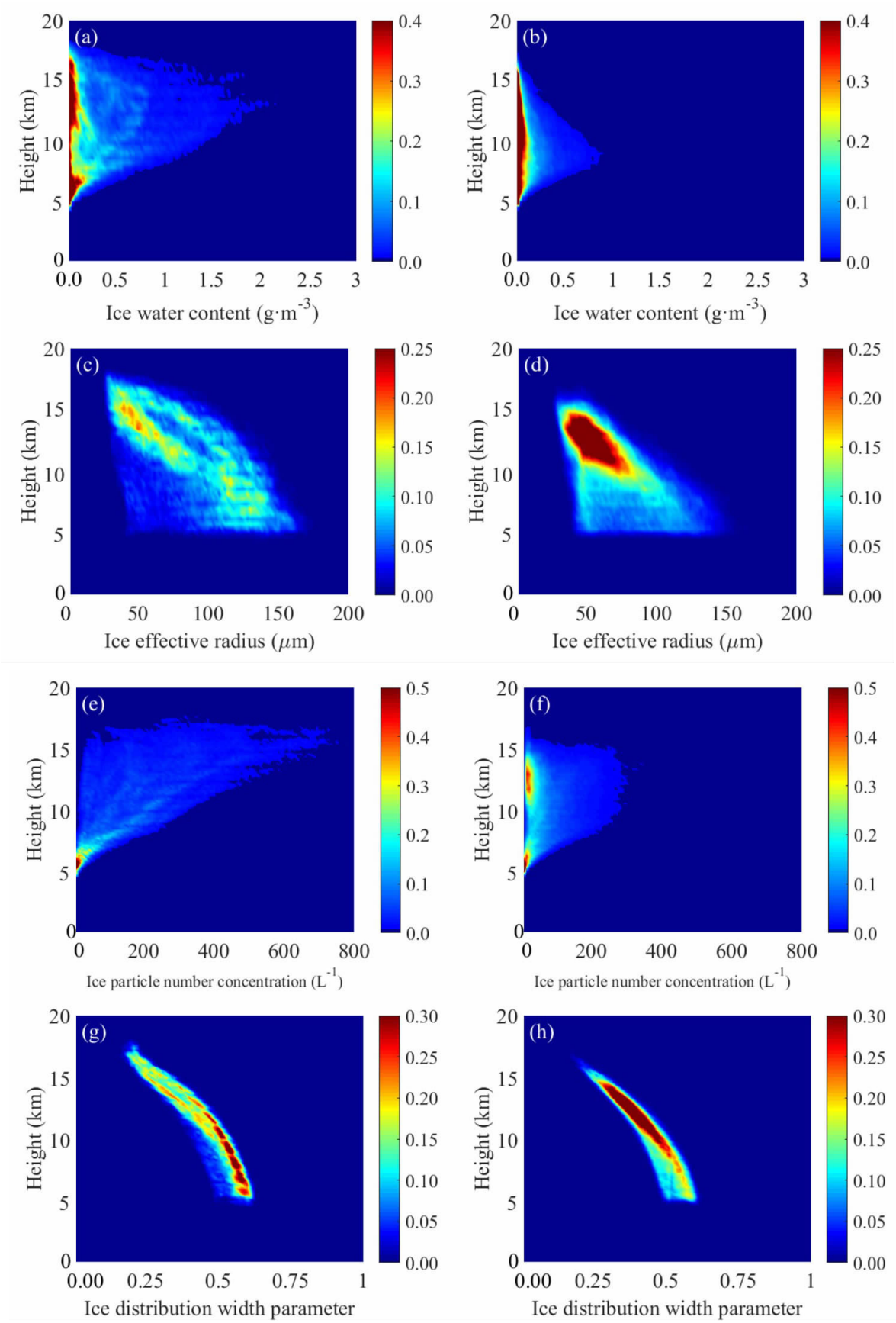

Figure 5. CFADs of ice cloud parameters in A1 and A5 regions at the mature stage. (a) ice water content in the A1 region; (b) same as in (a) but for the A5 region; (c) ice effective radius in the A1 region; (d) same as in (c) but for the A5 region; (e) ice particle number concentration in the A1 region; (f) same as in (e) but for the A5 region; (g) ice distribution width parameter in the A1 region; and (h) is the same as in (g) but for the A5 region.

21994-2017 China Academic Journal Electronic Publishing House. All rights reserved. http://www.cnki.net

stage. The radar reflectivity gradually drops off as the radial distance increases, which depicts the continuous weakening of convection intensity. At the developing and mature stages (Fig.3a and 3b), strong reflectivities extend to the altitude of 17 km, while they only extend to 12 km at the decaying stage (Fig.3c), during which the convective motion is greatly weakened and the TC goes to the end.

3.2 *Cloud occurrence probability*

The CloudSat 2B-CLDCLASS product classifies clouds into the eight types of cirrus (*Ci*), altostratus (*As*), altocumulus (*Ac*), stratocumulus (*Sc*), stratus (*St*), cumulus (*Cu*), nimbostratus (*Ns*), and deep convective (DC) by combining spaceborne active (CPR and CALIOP) and passive (MODIS) measurements, such as cloud base height, cloud layer temperature and upward radiance, liquid water path, and the presence or absence of precipitation. Fig.4 shows the CFAD of the CPR cloud classification at each stage in each region. DC covers the whole vertical scale of TCs and exhibits the largest occurrence probability almost everywhere, except for the altitude between 10 km to 15 km in the A4 and A5 regions where *Ci* is more prominent. The occurrence probability of DC falls at these altitude because of the larger probability of *Ci*. In the upper levels, outward flow brings thin *Ci* away from the storm center. The vertical stretching of *As* is the second largest after DC and its probability is relatively large above 7 km. *Sc* always appears in the lower levels with a small vertical scale. *Sc* occurs more frequently as the stage turns from developing to decaying as well as along a gradient from the A1 to A5 regions. *St* is scarce at all three stages and in all five regions. The occurrence probabilities and vertical distributions of *Ac*, *Cu*, and *Ns* have little variation at different stages or in different regions.

3.3 *Ice cloud parameters*

In the CloudSat 2B-CWC solution, the portion of the profile higher than -20 ℃ is considered as ice, while the protion of the profile lower than 0 ℃ is deemed pure liquid. Between -20 ℃ and 0℃ are mixed phase particles. Based on a forward physical model, the CloudSat 2B-CWC product retrieves microphysical parameters of ice clouds using active and passive remote sensing measurements together with a priori data (Austin et al.[36]). The model assumes that ice particles are characterized by a lognormal size distribution. The CloudSat product generally agree reasonably well with previous comparison studies. But large size particles violate the assumed particle size distribution and Mie effects lead to systematic errors (Wu et al. [37]; Heymsfield et al.[38]).

The CFADs of ice cloud parameters in the A1 and A5 regions at the mature stage are displayed in Fig.5. The ranges of CPR measurements are reasonably consistent with *in situ* observations (Ackerman [39]; Merritt and Wexler [40]; Houze et al.[41]). IWC climbs to a peak value of nearly 2.3 g m^{-3} at 13 km in the A1 region (Fig.5a), while it decreases to 0.9 g m^{-3} at 9 km in the A5 region (Fig.5b). Large probabilities of IWC occur at 5−7 km and 11−17 km in the A1 region, while they occur in the A5 region at 5−15 km. R_e peaks at the melting layer, with a value of 180 μm in the A1 region (Fig.5c) that decreases to 150 μm in the A5 region (Fig. 5d). With increases in the radial distance, the probability of large R_e (e.g., >100 μm) below 10 km becomes smaller while the probability of small R_e (e.g., <80 μm) above 10 km becomes larger. In the A1 region, the maximum N_T is 790 L^{-1} at approximately 15 km (Fig. 5e). This decreases to 330 L^{-1} at 14 km in the A5 region (Fig.5f). The distributions of ω in the A1 and A5 regions are similar, ranging from 0.25 to 0.6 (Fig.5g and 5h). Large values of ω are more easily seen in low altitudes or in outer regions. Small graupels are formed and lifted in the eyewall regions, then turn to ice crystals through s econdary nucleation (Cantrell and Heymsfield [42]). In A1 region, it is more difficult for the updraft to transport large particles. Therefore, IWC and R_e both decrease with height. In the A5 region, ice particles sink and aggregate, eventually forming stratiform precipitation (Black and Hallett[43]; Black and Hallett [44]).

3.4 *Moist static energy*

The moist static energy (MSE) describes the thermodynamic state of an air parcel. MSE is a combination of internal energy, potential energy, and latent energy. MSE can be defined mathematically as:

$$h = C_p T + gz + L_v q \quad (1)$$

where h, T, z, and q refer to MSE (kilojoule/ kilogram), temperature (Kelvin), height above the sea level (meters), and specific humidity (kilograms/ kilogram), respectively. C_p is the isobaric specific heat capacity, g is the acceleration of gravity, and L_v is the latent heat of vaporization.

Wong and Emanuel derived a preliminary method for TC intensity estimation [6], which was simplified by Luo, et al. as[5]:

$$MSW = \frac{T_S - T_O}{T_O}\Delta h \quad (2)$$

where T_s and T_o are the sea surface temperature (SST) and cloud top temperature, respectively, and Δh is the difference between the cloud top MSE of the eyewall and the outer region.

It can be inferred from Eq.(2) that the stronger the maximum wind in a granule, the larger the Δh. All granules are classified in two different ways: according to the stage and according to SSHWS. Radial distributions of cloud top MSE classified in these two ways are displayed in Fig.6, which shows reasonable agreement with Eq. (2). MSE is on a declining trend with the radial distance increasing in both panels. The maximum MSE all occur within 50 km of the storm center. In Fig. 6a, the maximum MSE of C1, C2&C3, and C4&C5 TCs are 358 kJ·kg^{-1}, 361 kJ·kg^{-1}, and 367

21994-2017 China Academic Journal Electronic Publishing House. All rights reserved. http://www.cnki.net

kJ·kg^{-1}, respectively. Outside a 300 km radius from the storm center, the values of MSE are all approximately 340-345 kJ·kg^{-1}. In Fig. 6b, Δh at the mature stage is the largest among the three stages. Δh at the developing stage is nearly the same as that at the decaying stage. However, the average value of MSE at the developing stage when TCs are intensifying is larger than that at the decaying stage when TCs are weakening.

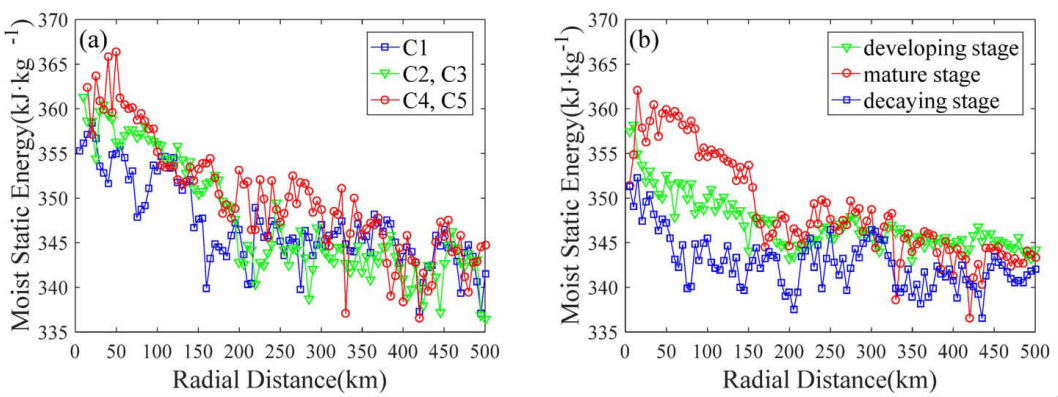

Figure 6. Radial distributions of cloud top moist static energy classified according to (a) SSHWS, (b) stage.

3.5 *Cloud base height and cloud thickness*

Via statistical analysis of the CloudSat 2B-GEOPROF-LIDAR product, cloud base height (CBH) and cloud thickness (CT) at each stage are shown in Fig.7. Overall, the CT in all three panels tends to diminish along the radial direction except for a slight growth within 50–100 km. However, the values of CBH exhibit a contrary trend. CBH is similar at different stages, and it slowly changes from 1 km up to 5 km as the radial distance increases. CT at the mature stage is significantly larger, attaining a maximum value of 14 km. Within 170 km of the storm center, CT is larger than 10 km. The descent of CT at the mature stage is steeper than those at the other two stages. Outside 350 km from the storm center, CT varies little at different stages, with a value of approximately 5–6 km. These phenomena demonstrate that convection in the inner region at this stage is stronger, and that it is less difficult to form precipitation.

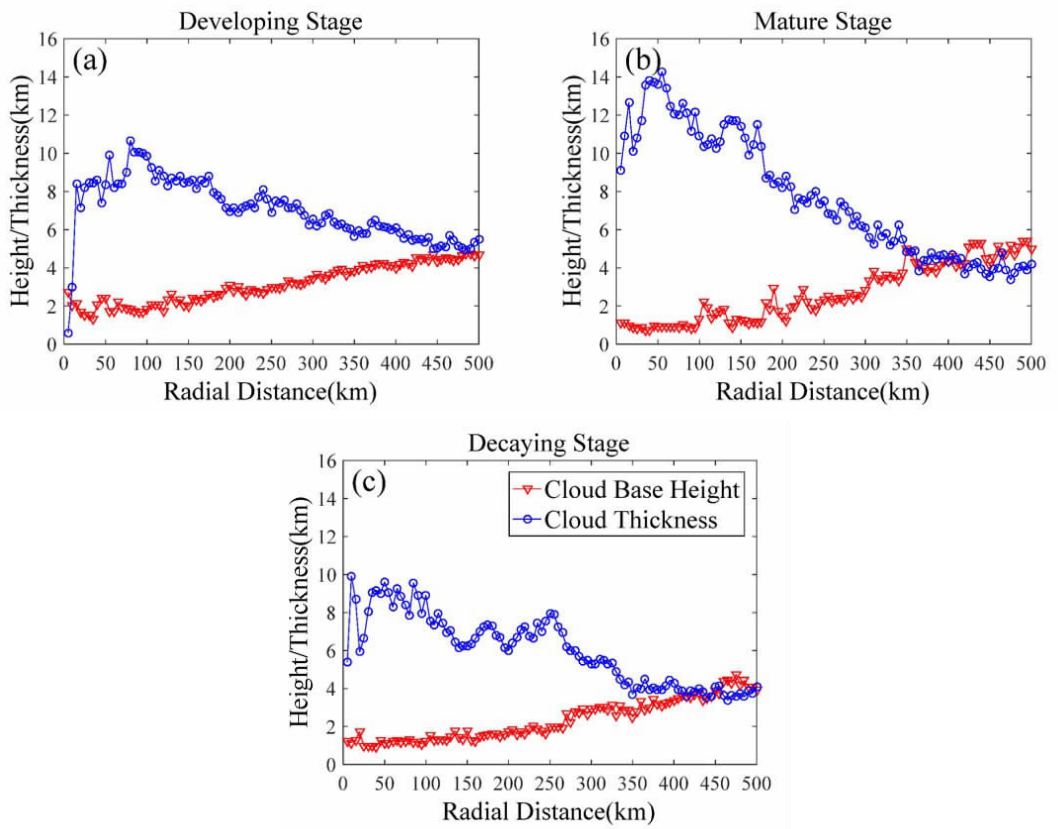

Figure 7. Radial distributions of CBH and CT at the (a) developing stage, (b) mature stage, and (c) decaying stage.

21994-2017 China Academic Journal Electronic Publishing House. All rights reserved. http://www.cnki.net

3.6 *Hydrometeor content and rain rate*

Figure 8 shows radial distributions of liquid water path (LWP), ice water path (IWP), water vapor (WV), and rain rate (RR). All the parameters diminish as the radial distance increases at all three stages, except for the region within 100 km. Water vapor declines slightly while the other three parameters dramatically change. LWP and IWP reach their maximum values within 50–100 km of the storm center, while rain rate reaches its maximum within 70 km. Within 80 km of the storm center, LWP, IWP, and rain rate at the mature stage are much larger than those at the other two stages. Outside a 200-km radius from the storm center, LWP, IWP, and rain rate are nearly the same at different stages.

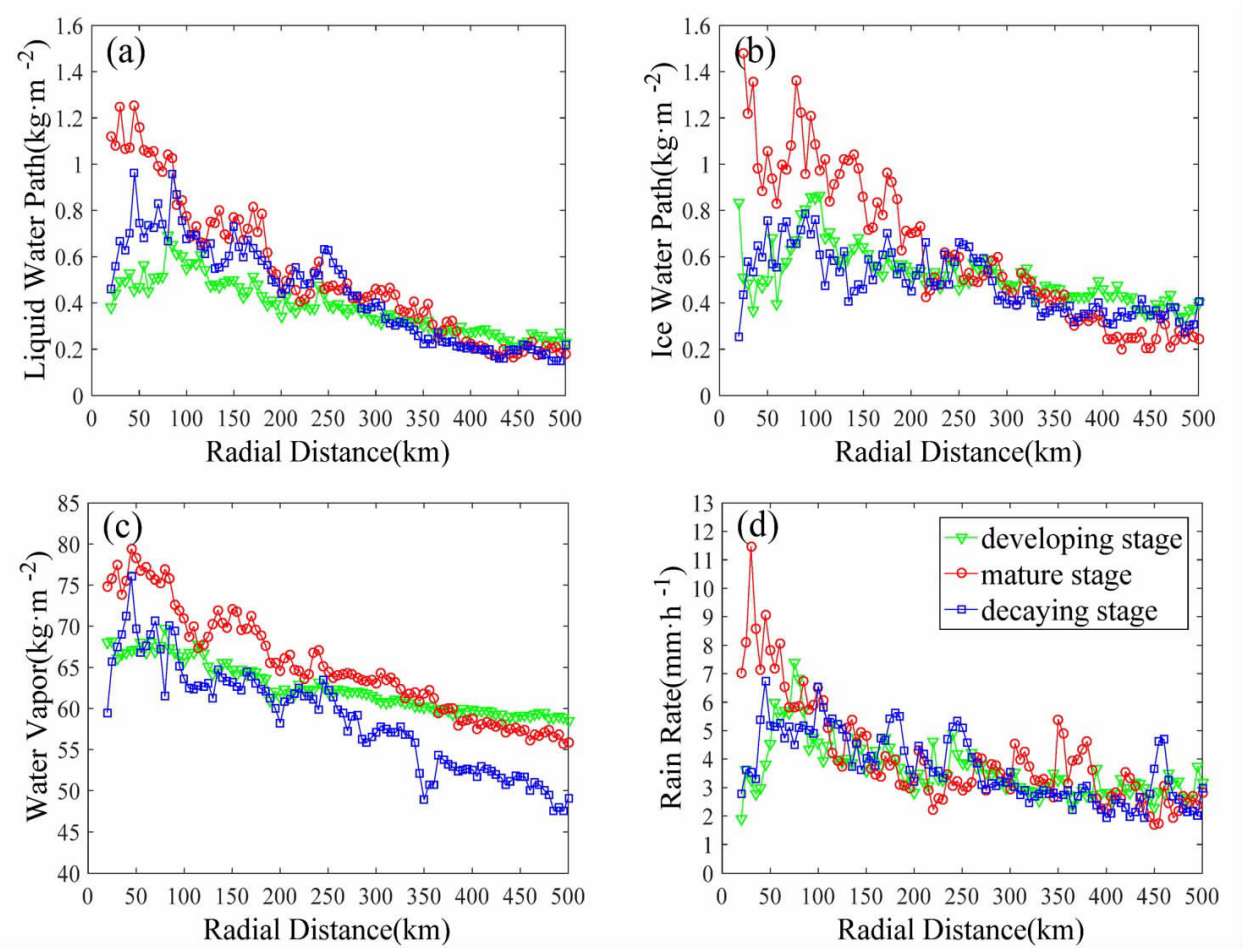

Figure 8. Radial distributions of (a) liquid water path, (b) ice water path, (c) water vapor, and (d) rain rate at three different stages.

3.7 *Maximum sustained wind and sea surface temperature*

Previous studies have suggested that the variation of sea water vapor flux, which is a function of sea surface wind and the difference between air temperature and SST, has a profound influence on the intensification of TCs. Zehr figured out that no TC had occurred when SST is less than 26 ℃ in the Western North Pacific [45]. Theories and observations all show that the maximum possible sustained wind (MPSW) is mainly limited by SST, and many other factors determine whether a TC reaches this potential (Evans [46]; Merrill [47]). To analyze the SST's impact on the upper bound of MSW, a scatter diagram of SST and MSW is presented in Fig.9. Only C1 and a limited number of C2 TCs are observed when SST is less than 26 ℃. When SST is larger than 26℃, the relationship between SST and MPSW exhibits nearly linear behavior.

4 SUMMARY AND FUTURE STUDIES

Although studies on TCs using satellite observations have been conducted for decades, the first spaceborne W-band CPR onboard CloudSat offers an unprecedented opportunity to analyze the internal structure of TCs. After eight years of operation, CloudSat has collected enough data for statistical research. By combining observations from other satellites of A-Train as well as atmospheric model data with CloudSat measurements, detailed structural characteristics can be studied. To date, no other spaceborne instrument has had the ability to penetrate TCs through a cross section.

In this study, we have statistically analyzed the cloud vertical structure of 94 Western Pacific TCs at

21994-2017 China Academic Journal Electronic Publishing House. All rights reserved. http://www.cnki.net

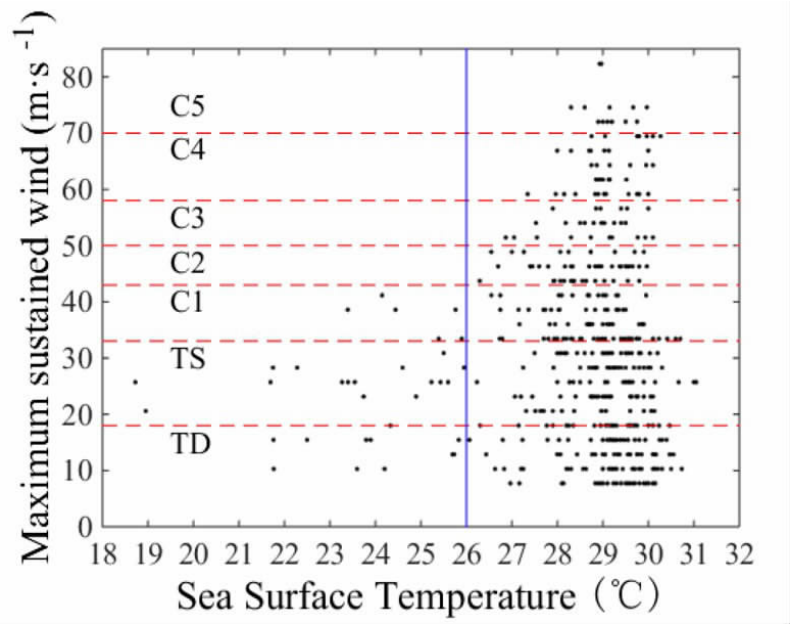

Figure 9. Scatter diagram of MSW and SST. Blue solid line indicates SST=26℃. Red dashed lines indicate border of different categories of SSHWS.

different stages within 500 km of the storm center. Radar reflectivity shows arc-like profiles and peaks at 5 km. Bright bands are found at this altitude, indicating melting layers. Radar reflectivity exhibits opposite distributions above and below the bright band. The echo intensity at the mature stage is greater than that at the other two stages. DC has the largest occurrence probability, except at 10-15 km in the outer region where cirrus has an advantage. *As* clouds are the second largest in vertical scale after DC. Distributions of *Ac*, *Cu*, and *Ns* at different stages have few distinctions. As the altitude increases, R_e and ω decrease while N_T increases. IWC attains its peak value at intermediate heights. MSE, CT, LWP, IWP, WV, and RR all diminish along the radial direction and are significantly larger at the mature stage. The average value of MSE at the developing stage is larger than that at the decaying stage.

CPR could detect vertical structure of clouds with high sensitivity and high spatial resolution. Meanwhile, its detecting precision is not affected by spatial and temporal changes. Such a vertical view is not available from passive (visible, infrared, and microwave) satellite devices or from active TRMM radar, which is not able to observe the upper regions of TCs because of its limited sensitivity (approximately 17 dBZ). CPR lacks spatial coverage due to the nature of its nadir-pointing detection and it is only able to provide information on a nadir cross section. The high-resolution information from CloudSat may be useful for validating TC models or for calibrating and refining remote sensing technologies with large spatial coverage. In addition, we can combine data from passive sensors onboard geostationary or polar-orbiting satellites with CloudSat observations to continuously and comprehensively analyze the cloud vertical structure in the future.

Acknowledgement: The CSTC Product is provided by the Naval Research Laboratory (NRL) and the CloudSat Data Processing Center (DPC) (http://reef.atmos.colostate.edu/~natalie/tc/). The best-track data was downloaded from Unisys Weather (http://www.weather.unisys.com/hurricane/).

REFERENCES:

[1] CHAN J C. Interannual and interdecadal variations of tropical cyclone activity over the western North Pacific [J]. Meteorol Atmos Phys, 2005, 89(1-4): 143-152.
[2] LANDSEA C W, VECCHI G A, BENGTSSON L, et al. Impact of Duration Thresholds on Atlantic Tropical Cyclone Counts* [J]. J Climate, 2009, 23(10): 2508-2519.
[3] ZHAN R, WANG Y, WU C-C. Impact of SSTA in the East Indian Ocean on the Frequency of Northwest Pacific Tropical Cyclones: A Regional Atmospheric Model Study [J]. J Climate, 2011, 24(23): 6227-6242.
[4] DUNION J P, THORNCROFT C D, VELDEN C S. The Tropical Cyclone Diurnal Cycle of Mature Hurricanes [J]. Mon Wea Rev, 2014, 142(10): 3900-3919.
[5] LUO Z, STEPHENS G L, EMANUEL K A, et al. On the use of CloudSat and MODIS data for estimating hurricane intensity [J]. Geosci Remote Sens Lett, IEEE, 2008, 5(1): 13-16.
[6] WONG V, EMANUEL K. Use of cloud radars and radiometers for tropical cyclone intensity estimation [J]. Geophys Res Lett, 2007, 34(12): L12811.
[7] CHEUNG K K W. A review of ensemble forecasting techniques with a focus on tropical cyclone forecasting [J]. Meteorol Appl, 2001, 8(3): 315-332.
[8] POROSEVA S V, LAY N, HUSSAINI M Y. Multimodel

21994-2017 China Academic Journal Electronic Publishing House. All rights reserved. http://www.cnki.net

Approach Based on Evidence Theory for Forecasting Tropical Cyclone Tracks [J]. Mon Wea Rev, 2010, 138(2): 405-420.
[9] DVORAK V F. Tropical Cyclone Intensity Analysis and Forecasting from Satellite Imagery [J]. Mon Wea Rev, 1975, 103(5): 420-430.
[10] RODGERS E B, CHANG S W, PIERCE H F. A Satellite Observational and Numerical Study of Precipitation Characteristics in Western North Atlantic Tropical Cyclones [J]. J Appl Meteorol Climatol, 1994, 33 (2): 129-139.
[11] KIDDER S Q, GOLDBERG M D, ZEHR R M, et al. Satellite Analysis of Tropical Cyclones Using the Advanced Microwave Sounding Unit (AMSU) [J]. Bull Amer Meteorol Soc, 2000, 81(6): 1241-1259.
[12] STERN D P, NOLAN D S. Reexamining the Vertical Structure of Tangential Winds in Tropical Cyclones: Observations and Theory [J]. J Atmos Sci, 2009, 66(12): 3579-3600.
[13] HENCE D A, HOUZE R A. Vertical Structure of Tropical Cyclones with Concentric Eyewalls as Seen by the TRMM Precipitation Radar [J]. J Atmos Sci, 2011, 69(3): 1021-1036.
[14] HENCE D A, HOUZE R A. Vertical Structure of Tropical Cyclone Rainbands as Seen by the TRMM Precipitation Radar [J]. J Atmos Sci, 2012, 69 (9): 2644-2661.
[15] MILLER S D, FORSYTHE J M, PARTAIN P T, et al. Estimating Three-Dimensional Cloud Structure via Statistically Blended Satellite Observations [J]. J Appl Meteorol Climatol, 2013, 53(2): 437-455.
[16] KOVACS T A, MCCORMICK M P. Observations of Typhoon Melissa during the Lidar In-Space Technology Experiment (LITE) [J]. J Appl Meteorol Climatol, 2003, 42(7): 1003-1013.
[17] YOKOYAMA C, TAKAYABU Y N. A Statistical Study on Rain Characteristics of Tropical Cyclones Using TRMM Satellite Data [J]. Mon Wea Rev, 2008, 136(10): 3848-3862.
[18] STEPHENS G L, VANE D G, BOAIN R J, et al. THE CLOUDSAT MISSION AND THE A-TRAIN [J]. Bull Amer Meteorol Soc, 2002, 83(12): 1771-1790.
[19] STEPHENS G L, VANE D G, TANELLI S, et al. CloudSat mission: Performance and early science after the first year of operation [J]. J Geophys Res, 2008, 113 (D8): D00A18.
[20] MITRESCU C, MILLER S, HAWKINS J, et al. Near-real-time applications of CloudSat data [J]. J Appl Meteorol Climatol, 2008, 47(7): 1982-1994.
[21] MATROSOV S Y. CloudSat measurements of landfalling hurricanes Gustav and Ike (2008) [J]. J Geophys Res, 2011, 116(D1): D01203.
[22] YUTER S E, HOUZE R A. Three-dimensional kinematic and microphysical evolution of Florida cumulonimbus. Part II: Frequency distributions of vertical velocity, reflectivity, and differential reflectivity [J]. Mon Wea Rev, 1995, 123(7): 1941-1963.
[23] DURDEN S L, TANELLI S, DOBROWALSKI G. CloudSat and A-Train observations of tropical cyclones [J]. Open Atmos Sci J, 2009, 3(1): 80-92.
[24] TOURVILLE N, STEPHENS G, DEMARIA M, et al. Remote Sensing of Tropical Cyclones: Observations from CloudSat and A-Train Profilers [J]. Bull Amer Meteorol Soc, 2015, 96(4): 609-622.
[25] KANTHA L. Time to replace the Saffir-Simpson hurricane scale? [J]. Eos, Transactions American Geophysical Union, 2006, 87(1): 3-6.
[26] CHAN J C L, YIP C K M. Interannual variations of tropical cyclone size over the western North Pacific [J]. Geophys Res Lett, 2003, 30(24): 2267.
[27] CHAN K T F, CHAN J C L. Size and Strength of Tropical Cyclones as Inferred from QuikSCAT Data [J]. Mon Wea Rev, 2012, 140(3): 811-824.
[28] CHAVAS D R, EMANUEL K A. A QuikSCAT climatology of tropical cyclone size [J]. Geophys Res Lett, 2010, 37(18): L18816.
[29] WADA A, USUI N, SATO K. Relationship of maximum tropical cyclone intensity to sea surface temperature and tropical cyclone heat potential in the North Pacific Ocean [J]. J Geophys Res, 2012, 117(D11): D11118.
[30] LIU K S, CHAN J C L. Size of Tropical Cyclones as Inferred from ERS-1 and ERS-2 Data [J]. Mon Wea Rev, 1999, 127(12): 2992-3001.
[31] MASUNAGA H, SATOH M, MIURA H. A joint satellite and global cloud-resolving model analysis of a Madden-Julian Oscillation event: Model diagnosis [J]. J Geophys Res, 2008, 113(D17): D17210.
[32] DODSON J B, RANDALL D A, SUZUKI K. Comparison of observed and simulated tropical cumuliform clouds by CloudSat and NICAM [J]. J Geophys Res, 2013, 118(4): 1852-1867.
[33] SASSEN K, MATROSOV S, CAMPBELL J. CloudSat spaceborne 94 GHz radar bright bands in the melting layer: An attenuation-driven upside-down lidar analog [J]. Geophys Res Lett, 2007, 34(16): L16818.
[34] HUANG Y, PROTAT A, SIEMS S T, et al. A-Train Observations of Maritime Midlatitude Storm-Track Cloud Systems: Comparing the Southern Ocean against the North Atlantic [J]. J Climate, 2014, 28(5): 1920-1939.
[35] HOUZE R A. Clouds in Tropical Cyclones [J]. Mon Wea Rev, 2010, 138(2): 293-344.
[36] AUSTIN R T, HEYMSFIELD A J, STEPHENS G L. Retrieval of ice cloud microphysical parameters using the CloudSat millimeter-wave radar and temperature [J]. J Geophys Res, 2009, 114(D8): D00A23.
[37] WU D L, AUSTIN R T, DENG M, et al. Comparisons of global cloud ice from MLS, CloudSat, and correlative data sets [J]. J Geophys Res, 2009, 114(D8): D00A24.
[38] HEYMSFIELD A J, PROTAT A, BOUNIOL D, et al. Testing IWC Retrieval Methods Using Radar and Ancillary Measurements with in Situ Data [J]. J Appl Meteorol Climatol, 2008, 47(1): 135-163.
[39] ACKERMAN B. Some Observations of Water Contents in Hurricanes [J]. J Atmos Sci, 1963, 20(4): 288-298.
[40] MERRITT E S,WEXLER R. CIRRUS CANOPIES IN TROPICAL STORMS [J]. Mon Wea Rev, 1967, 95(3): 111-120.
[41] HOUZE R A, MARKS F D, BLACK R A. Dual-Aircraft Investigation of the Inner Core of Hurricane Norbert. Part II: Mesoscale Distribution of Ice Particles [J]. J Atmos Sci, 1992, 49(11): 943-963.
[42] CANTRELL W, HEYMSFIELD A. Production of Ice in Tropospheric Clouds: A Review [J]. Bull Amer Meteorol Soc, 2005, 86(6): 795-807.

21994-2017 China Academic Journal Electronic Publishing House. All rights reserved. http://www.cnki.net

[43] BLACK R A, HALLETT J. Observations of the Distribution of Ice in Hurricanes [J]. J Atmos Sci, 1986, 43(8): 802-822.
[44] BLACK R A, HALLETT J. Electrification of the Hurricane [J]. J Atmos Sci, 1999, 56(12): 2004-2028.
[45] ZEHR R. Satellite diagnosis of tropical cyclones [C]// 3rd Conference on Satellite Meteorology and Oceanography, 1988: 241-246.
[46] EVANS J L. Sensitivity of Tropical Cyclone Intensity to Sea Surface Temperature [J]. J Climate, 1993, 6 (6): 1133-1140.
[47] MERRILL R T. Environmental Influences on Hurricane Intensification [J]. J Atmos Sci, 1988, 45(11): 1678-1687.

Citation: LI Guan-lin, YAN Wei, HAN Ding et al. Applications of the CloudSat tropical cyclone product in analyzing the vertical structure of tropical cyclones over the western Pacific [J]. J Trop Meteorol, 2017, 23(1): 1-14.

21994-2017 China Academic Journal Electronic Publishing House. All rights reserved. http://www.cnki.net